ACS Photonics

Letter

pubs.acs.org/journal/apchd5

Free-Standing Silicon Nanogratings for Extreme UV Rejection

Alex F. Kaplan,[‡] Jason A. Gilbert,[†] Rachel Trabert,[†] Thomas H. Zurbuchen,*[,†] and L. Jay Guo*[,‡]

[†]Atmospheric, Oceanic and Space Sciences, Zurbuchen University of Michigan, 2455 Hayward Street, Ann Arbor, Michigan 48109, United States

[‡]Electrical Engineering and Computer Science, University of Michigan, 1301 Beal Avenue, Ann Arbor, Michigan 48109, United States

ABSTRACT: The integration of compact, sturdy, and lightweight sensors into satellites for measurement of low-density plasmas has been hindered by their inherent sensitivity to extreme UV photons. Silicon nanograting structures that reject extreme UV light while allowing particles to pass through have improved on previous gold gratings in terms of stability and ease of fabrication, but comparable UV rejection was not attained since Si acts as a plasmonic material in the extreme UV. In order to alter the plasmonic properties of the structure, atomic layer deposition technology was utilized during fabrication, and extreme UV transmission comparable to previous results was achieved. This work reports the fabrication and measurement of coated, free-standing Si nanogratings created over a large area using nanoimprint lithography. With reduction in defect density, these structures could outperform current gold gratings as UV filters in space-based mass spectrometry systems.

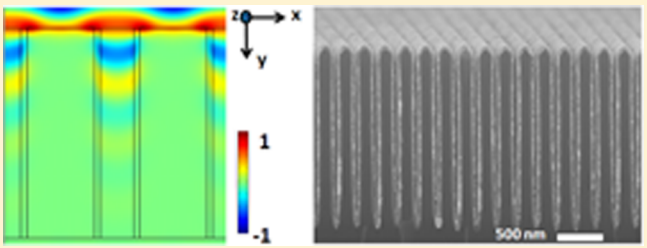

KEYWORDS: *nanogratings, polarizer, plasmonics, nanoimprint, mass spectrometry*

In situ measurements of solar wind, the low-density plasma emanating from the Sun, continue to be among the most sought after data for gaining further understanding of the workings and origins of our solar system. In situ measurements are typically conducted by instruments launched into space as part of a multifaceted mission, limiting the size, complexity, and cost associated with the sensor. Furthermore, the measurement environment for detection of low-energy neutrals and ions is inhospitable due to the abundance of extreme UV (EUV) photons from the Sun, which degrade the signal-to-noise ratio. In particular, high-energy Lyman-α photons ($\lambda \approx 121.6$ nm, Ly-α) from excited hydrogen emission in the Sun can create substantial background noise in particle sensors. The Ly-α photon flux at Earth is approximately 5×10^{11} cm^{-2} s^{-1}, which is orders of magnitude greater than solar wind flux ($\sim 10^6$–10^7 cm^{-2} s^{-1}), requiring sensors that greatly reduce the transmission of Ly-α photons.[1] Depending on the location of measurements relative to the Sun, previous works have targeted extremely low Ly-α transmission, on the order of 10^{-6}–10^{-10} or lower, in order to adequately measure both ion and neutral particle flux.[2,3]

To remove the substantial EUV background noise, designs are often used where the trajectories of incoming ions or ionized neutrals are altered by electromagnetic fields and guided to a sensor while light travels separately into light-attenuating traps For example, the low-energy (10–750 eV) neutral atom (LENA) imager on the imager of magnetosphere-to-aurora global exploration (IMAGE) uses a hemispherical electrostatic deflection system to guide neutral particles after being ionized by a charge-exchange conversion surface.[4] While the particles traverse a path that curves ~270° to a detector, photon trajectories are unaltered and continue on to strike interior surfaces that are blackened using light-absorbent coatings common for space hardware. The medium-energy neutral atom (MENA) imager, which measures neutral atoms in the energy range from 1 to 30 keV, was also flown on the IMAGE mission.[1] Without an electrostatic deflection system, the detectors on this sensor are directly in the line of sight of the entrance aperture and, therefore, highly susceptible to triggering by EUV. To reject the incident photon flux, yet still maintain a high geometric transparency to permit the targeted neutral atoms to enter the sensor, a high aspect ratio, free-standing gold grating structure was placed at the entrance aperture. Building on earlier research in EUV rejection[5,6] the structure was fabricated with a 200 nm period, approximately 50 nm wide slits, and 400 nm depth by electroplating over photoresist patterned using interferometric lithography.[7] Since the plasmon energy of gold is in the visible range, the material acts as an effective EUV absorber, while the slits still allow particles to pass through and be collected for detection. The mean value of Ly-α transmission measurements for the 15 flight gratings was 6×10^{-6}.[1] However, the structural weakness of gold gratings prevents the scalability of this nanograting design for higher aspect ratios and reduced EUV transmission, limiting widespread use in further space missions. In order to achieve more precise measurements of ions and neutrals in environments with higher Ly-α intensity, continued improvement in EUV rejection must be achieved.

More recently, a high aspect ratio, free-standing nanograting structure was fabricated entirely from silicon in order to greatly increase the overall structural integrity and grating depth.[3,8]

Received: January 17, 2014
Published: June 11, 2014

Furthermore, by utilizing nanoimprint lithography and deep reactive ion etching (DRIE) techniques, structures have been fabricated over larger areas with aspect ratios near 60:1, which could theoretically improve the efficiency and EUV rejection over the previous gold grating structures.[9,10] While fabricated Si structures did not have all fabrication defects plugged as was done with their counterparts flown in MENA, experimental measurements of UV transmission were still relatively low, on the order of 10^{-4}. However, given the variations in grating dimensions during fabrication and optical properties of Si, further improvements need to be made to achieve much lower EUV transmission than MENA gratings.

To reduce EUV transmission, a more thorough analysis and experiment was undertaken to investigate ideal materials and feature sizes to achieve Ly-α transmission on the order of 10^{-6} or less while continuing to utilize the stability provided by the free-standing Si structure. Unlike most metals, which have plasmon frequencies at visible wavelengths,[11,12] Si has a reported volume plasmon energy of approximately 16 eV ($\lambda_p \approx 77$ nm).[13] At Ly-α, $\lambda = 121.6$ nm, this means that Si has a refractive index much less than $n = 1$ and relatively high extinction coefficient κ (relating to absorption loss) when compared with Au at the same wavelength, similar to typical optical properties for metals at visible wavelengths (Table 1). This will greatly change the mode of light propagation and absorption when Ly-α passes through a Si grating as compared with a Au grating.

Table 1. Table of Complex Index of Refraction ($n + i\kappa$) and Calculated Permittivity ($\varepsilon_1 + i\varepsilon_2$ where $\varepsilon_1 = n^2 - \kappa^2$ and $\varepsilon_2 = 2n\kappa$) for Selected Materials at $\lambda = 121.6$ nm[10,11]

material	n	κ	ε_1	ε_2
Si	0.295	1.30	−1.60	0.767
Al	0.044	1.18	−1.39	0.104
Au	1.265	0.967	0.670	2.447
Pt	1.350	1.18	0.430	3.186
Al_2O_3	2.519	0.629	5.950	3.169

In the near-visible wavelength regime, Au and other metals have similar properties (low n, high κ), which has led to their study in metal−insulator−metal (MIM) waveguide structures, also known as plasmonic or metallic "slot" waveguides.[14−18] These structures consist of a dielectric "core" surrounded by metallic "cladding". As opposed to typical waveguide structures such as optical fibers with dielectric cladding, these plasmonic waveguides can effectively confine and guide light with wavelengths larger than the core thickness, making them particularly desirable for applications such as on-chip photonic waveguiding. The metallic walls of the waveguide allow free-space optical modes to be coupled into surface electron oscillations with highly confined electromagnetic fields. Given the waveguide geometry and the wavelength-dependent optical properties of the materials in the MIM structure, solutions to Maxwell's equations can be derived for supported waveguide modes and a propagation length can be calculated. Most studies have primarily focused on increasing light propagation length by reducing loss, but similar theories can be used to investigate increased absorption for our application in periodic waveguide structures such as free-standing nanogratings.

Given the optical properties of Si in the EUV regime, solutions to Maxwell's equations can be used to demonstrate that Ly-α light couples to modes with long propagation lengths as opposed to those in Au gratings, thus requiring much deeper grating structures to be fully absorbed. This would require extremely narrow and deep Si trenches in order to fully absorb Ly-α photons. Instead, this work demonstrates that atomic layer deposition (ALD)[19] can be used to coat prefabricated, free-standing Si nanograting structures in order to increase absorption of the propagating modes. A fabricated Si nanograting with a 20 nm Pt coating is demonstrated to achieve Ly-α transmission on the order of 10^{-4}, with simulations showing that improvements in fabrication and defect reduction can lead to even more promising results. This work also demonstrates the use of Si as a plasmonic material in the EUV regime, making it possible to use as an alternative to Al in wire grid polarizers for EUV wavelengths.[20,21]

DESIGN AND SIMULATION

Since the optical properties of Si are "metallic" at EUV wavelengths, simulations of Ly-α UV at transverse electric (TE) and transverse magnetic (TM) polarization can be performed in a MIM, slot waveguide scheme using similar methods as outlined in ref 14 (see Figure 2 for polarization definitions).

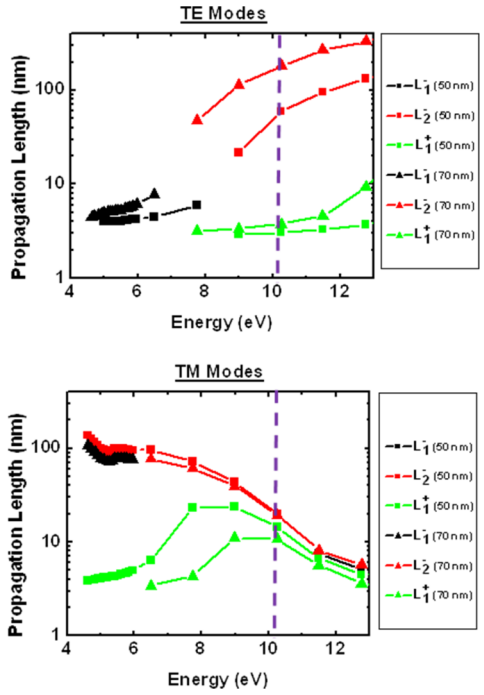

Figure 1. Propagation length (log) for a given photon energy through a Si−air−Si waveguide for both TE and TM propagating modes. Two antisymmetric (L^-) modes and one symmetric (L^+) mode are plotted for two air core widths (50 and 70 nm).

The wavelength-dependent optical properties of Si are used as the "metallic" cladding material, while an air core of varying thickness is assumed for geometry variation. Using these parameters, solutions to Maxwell's equations can be derived, including the propagation constant (β) of the supported modes. Using the imaginary component of the propagation constant, we can plot the propagation length, which is defined as the point of e^{-1} reduction in intensity. In this case, given two possible core widths (50 and 70 nm) supported symmetric (even) and antisymmetric (odd) modes are plotted for TE and TM polarizations (Figure 1).

dx.doi.org/10.1021/ph500018b | ACS Photonics 2014, 1, 554−559

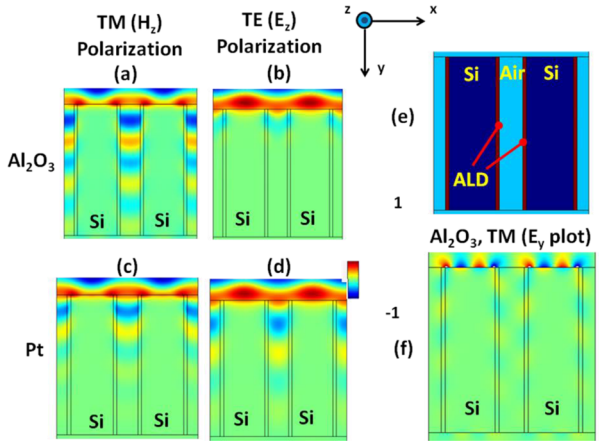

Figure 2. COMSOL field profile simulations for 400 nm thick, 200 nm period gratings with 60 nm trench widths (TW) and 10 nm ALD coatings. Plots show the *z*-component of magnetic (H) or electric (E) fields for (a, b) TM and TE polarizations for Al_2O_3-coated Si gratings and (c, d) TM and TE polarizations for Pt-coated gratings. The refractive index profile for a general ALD-coated structure (e) and the *y*-component of the electric field for the Al_2O_3-coated grating (f) demonstrate a propagating SPP mode.

Similar to ref 14, the antisymmetric mode propagation lengths (L^-) plotted in Figure 1 are longer than symmetric mode propagation lengths (L^+). For TE modes, decreasing core width (i.e., width of the air slit) is also shown to reduce propagation length, but core widths of <50 nm would be required in order to achieve an order of magnitude improvement in Ly-α (~10 eV) rejection over Si nanograting gratings that can currently be fabricated. Air core widths in actual structures can also vary along the propagation length due to imperfections in high aspect ratio Si etching, leading to increased EUV transmission (see Sections 3 and 4). It is also apparent that TE transmission through the grating structure would dominate, with propagation lengths nearly reaching an order of magnitude higher than TM modes, since TM modes are coupling to plasmon waveguide modes in the high-loss Si cladding material. These TM modes are therefore well suppressed in Si nanogratings, even with larger trench widths. Assuming a fixed grating depth, the propagation lengths of TE modes will need to be reduced in order to reduce the overall EUV transmission of Si gratings.

The reduction of TE transmission intensity by the tuning of Si nanograting dimensions would require much narrower core widths and deeper grating structures, which are difficult to fabricate. Variations in the air slit width throughout the grating depth created during the Si etch process can also lead to orders of magnitude variation from the simulation results presented. In recent years, major improvements in atomic layer deposition technology allow structures to be coated with angstrom-level precision, even with aspect ratios as high as those in fabricated Si nanogratings. This would essentially create a graded or metal−multi-insulator−metal (MMIM) waveguide, which has also been investigated for improving propagation lengths.[22] In

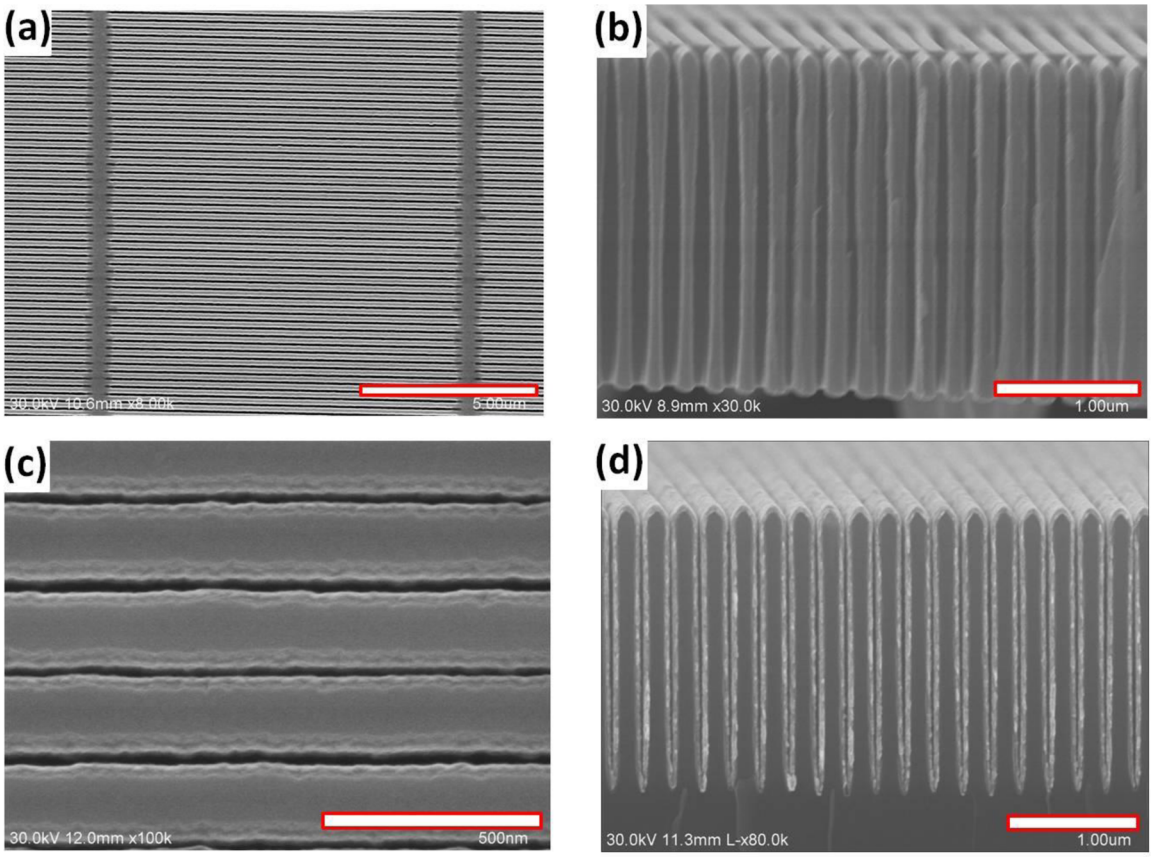

Figure 3. SEM images of fabricated Si nanograting structures. (a) Top view showing 220 nm period gratings with 75 nm trench widths (~10 μm perpendicular support bars) (5 μm scale bar). (b) Side view of free-standing Si grating (1 μm scale bar). (c) Top view showing ~20 nm Al_2O_3 ALD coating (500 nm scale bar). (d) Side view demonstrating conformal coating of Pt on high-aspect-ratio Si grating (1 μm scale bar).

dx.doi.org/10.1021/ph500018b | *ACS Photonics* 2014, 1, 554−559

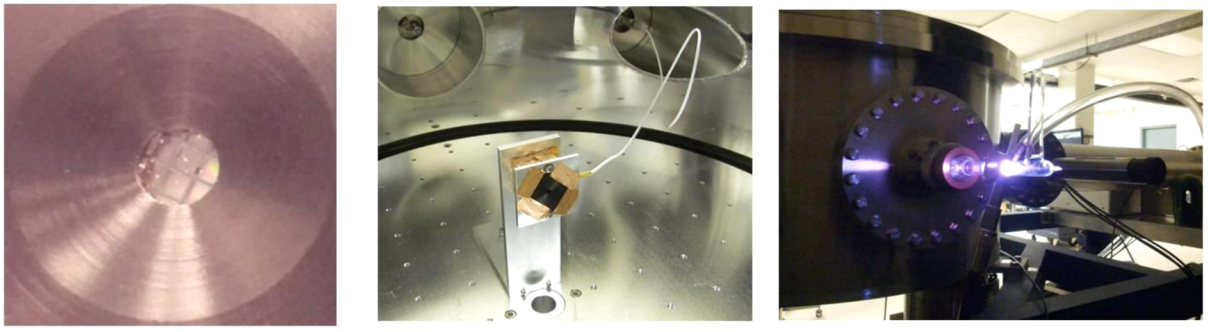

Figure 4. Images of Ly-α transmission measurement setup. (Left) 3 mm diameter aperture plate with UV grating sample attached. This image also shows visible defects on a fabricated nanograting sample. (Center) Image inside a vacuum chamber showing grating sample attached to aperture and photodiode. (Right) EUV microwave lamp source showing visible light emission.

this work, the effects of a high-index and low-index dielectric coating were investigated in order to increase light confinement at the center of the core and reduce losses to the cladding material. Similar to the methods discussed above, by assuming tangential field continuity at the boundaries of the materials, Maxwell's equations were solved to plot the field profile in these multilayered structures and investigate the effects on the propagation constant. According to the results of Figure 5 in ref

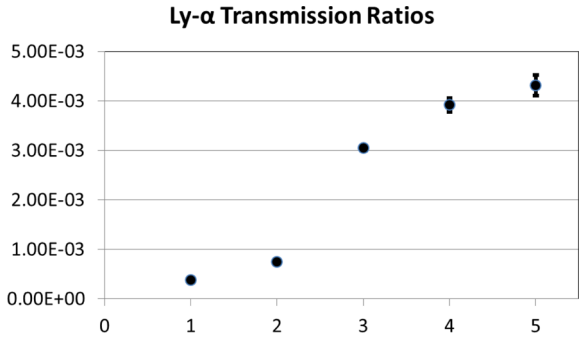

Figure 5. Transmisson for Ly-α through the gratings listed in Table 2. Error bars indicate ± 1 standard deviation.

22, coating the sidewalls of the MIM waveguide with a higher index material than air can increase optical confinement of propagating TE waveguide modes near the Si walls. If this material also had high loss at the targeted wavelength, confinement in this region could lead to greatly increased attenuation of the propagating mode. Al_2O_3 and Pt were chosen for experimentation since they have $n > 1$ (see Table 1), and mature deposition precursors and coating results have already been demonstrated.[19]

To investigate the effect on wave propagation in ALD-coated Si nanogratings, finite-element analysis software simulations assuming periodic boundary conditions were performed at $\lambda = 121.6$ nm using COMSOL MULTIPHYSICS. Structures with similar dimensions to MENA Au gratings (400 nm depth, 200 nm period, 50 nm trench widths) and optical properties given in Table 1 were obtained to confirm the affects of 10 nm thick, high-index ALD coatings on the gratings (Figure 2). Since Al_2O_3 has a much higher refractive index than Pt at Ly-α, the field profile simulations clearly show the expected increase in attenuation of the TE mode in Al_2O_3-coated gratings (Figure 2b) as compared to Pt-coated (Figure 2d) due to the increased confinement of the waveguide mode near the Si surface. However, this improvement in TE mode attenuation appears to be balanced by the improved propagation of TM antisymmetric modes, as predicted in ref 22. Comparing Figure 2a with Figure 2c shows much stronger TM mode propagation for Al_2O_3-coated gratings, and the Figure 2f plot of the electric field for TM modes shows a clear antisymmetric profile. With increased grating depth and narrower trench widths created by thicker ALD coatings, much greater attenuation of Ly-α flux can theoretically be achieved by either Pt- or Al_2O_3-coated gratings when compared with previously tested Si nanogratings. For example, the Pt-coated structure in Figure 2d has simulated TE-polarized Ly-α transmission of $\sim 1 \times 10^{-5}$; this would roughly equate to a propagation length of ~35 nm. If the core width can be controlled to this dimension and fabrication defects can be reduced or plugged, a 2.5 μm depth grating could theoretically reach $e^{-2.5/0.035} \approx 10^{-31}$ transmission of the TE mode.

EXPERIMENTAL SECTION

Fabrication Procedure. The fabrication process to create the free-standing Si grating structures is briefly outlined below. More detailed information and diagrams of the fabrication procedure and DRIE recipe are presented in refs 3, 8, and 9. The procedure primarily utilized nanoimprint lithography for patterning in order to generate the periodic structures over a large area. Unlike previous interference lithography techniques to produce Au gratings, nanoimprint lithography can be performed over larger areas and possibly refined to a roll-to-roll manufacturing process.[23] DRIE was performed using a modified Bosch process, which uses alternating etch and deposition cycles with precise timing and gas regulation in order to selectively etch Si in a vertical direction.

A silicon-on-insulator (SOI) wafer was chosen with a desired device layer thickness (i.e., 2.5 or 4.5 μm), which would eventually become the grating depth (waveguide length). Nanoimprint lithography using a Nanonex NX2000 tool was used to create 220 nm period grating structures in imprint resist (mr-I 8030) over an approximate 1 in. × 1 in. area and transferred into an already deposited thin oxide layer using reactive ion etching. An 11 μm period support structure was also patterned perpendicular to the 220 nm period grating (see Figure 3a). This oxide structure would be used as the future mask for the top grating DRIE step. After the oxide mask was fully defined on the device side of the SOI chip, the sample was flipped over and photolithography was used to define the large back-side support structure. Along with stability, this step defines the free-standing regions of the Si grating, which will be patterned in the device layer.

dx.doi.org/10.1021/ph500018b | ACS Photonics 2014, 1, 554−559

Finally, the sample was again flipped to etch the device layer nanograting using a Bosch process DRIE recipe that was slightly modified from ref 9 (temperature −15 °C, pressure 7.5 mT, deposition 1 s, 150 sccm C_4F_8, 2000 W coil; etch 6.5 s, 80 sccm C_4F_8, 200 SF_6, 1100 W coil, 30−48 W bias (linear ramp)). Delay times for heat dissipation were also added between etch and deposition. A typical etch time for a 2.5 μm thick device layer was approximately 12 min. Al_2O_3 ALD coatings were performed using an Oxford OpAL ALD tool, while contacts at NIST deposited Pt using an Oxford FlexAL ALD tool.

Measurement Setup. Images showing some of the general measurement setup are given in Figure 4. The measurement setup to quantify Ly-α transmission through grating structures was created using a EUV Opthos Instrument microwave cavity lamp with a hydrogen−argon bulb that emits a strong Ly-α peak along with other components of visible light.[24] Transmission intensity through a sample was taken by measuring current excited in a 1 cm^2 NIST-calibrated International Radiation Detectors IRD AXUV-100G photodiode. Samples were mounted on a 3 mm diameter circular aperture and placed over the photodiode. To avoid possible contamination of the UV measurement with wavelengths in the visible range, the light from the UV lamp was passed through a Pelham Optics 122FNB EUV narrow bandpass filter prior to reaching the nanograting (passing ∼15% of 122 nm EUV with a full-width at half-maximum of 20 nm). Current measurements from the photodiode were taken using a Keithley 6514 electrometer and were performed in a vacuum chamber under $\sim 10^{-5}$−10^{-6} Torr to avoid absorption of UV by air or residual gases.

Despite the bandpass filter used, some visible light could still be detected (although greatly attenuated), so transmission results through gratings alone were compared with transmission through gratings mounted on fused silica substrates. Reference measurements with an open aperture, a fused silica sample, and a 2.5 μm thick Si device layer were also taken for comparison (this sample was created from the same SOI wafers above, but did not have a patterned grating). Since thick fused silica will absorb or reflect the UV component of the lamp, measurements taken through a given grating with and without fused silica could be compared in order to determine what portion of the measured current in the photodiode is due to the EUV transmission.

RESULTS AND DISCUSSION

Using the process outlined above, free-standing gratings were fabricated in a released Si layer of a SOI chip with an approximately 220 nm period, 75 nm trench width, and both 2.5 and 4.5 μm depth. Gratings were coated with varying thicknesses of Al_2O_3 or Pt through ALD (∼10−20 nm) in order to investigate the effects of trench width, material properties, and depth on Ly-α extinction capability of the structure. Figure 3a and b show an example of a 2.5 μm depth, free-standing Si grating sample fabricated over a large area. As mentioned above, this Si nanograting was able to be reproducibly fabricated with a 75 nm trench width, but this trench width still allows for deep propagation of the TE mode into the structure, and width variations caused by the Si etch lead to further increases in EUV transmission. The etch depth of the Si grating would need to be greatly increased in order to achieve or improve on the $\sim 10^{-6}$ Ly-α transmission through MENA gratings. Figure 3b shows the variation in trench width below the surface of the structure (typically referred to as "bowing"), which can lead to increased Ly-α transmission. Figure 3c and d show examples of ALD coating on etched Si nanograting structures and the uniform coverage that could be achieved. Figure 3c demonstrates a ∼20 nm coating of Al_2O_3, reducing the initial trench width of the sample to <40 nm. Cross-section images were not taken of free-standing structures due to the time and cost put into fabrication, but Figure 3d shows an example of the uniform coating on an entire 2.5 μm depth grating etched into a Si wafer. While bowing is not as pronounced in this sample, one can see that trench widths are greatly reduced throughout the entire grating depth, but variation of the air core width is still present.

Due to the lack of access to a vacuum monochromator capable of isolating Ly-α to test the transmission on fabricated grating structures, the measurement setup outlined in Section 3 was developed in order to utilize an available Ly-α source and reject visible light, which can ruin any quantification of UV rejection. Various gratings and samples were placed in front of a photodiode under vacuum while a Ly-α source was shined onto the samples. Results were compared with transmission through fused silica samples in order to effectively account for visible light generated by the Ly-α source (see Section 3).

Figure 5 shows the Ly-α transmission for 5 gratings of various coatings and depths. Details on each grating are given in Table 2. The lowest transmission (3.8×10^{-4}) was observed in grating 1, which had trenches 2.5 μm deep and was coated with a 20 nm layer of Pt, as expected from simulations above. Of the gratings coated with Al_2O_3, grating 2, which had 4.5 μm deep trenches, was best able to suppress the UV transmission due to the increased length that UV propagates through the structure. Between gratings 3 and 4, which both had 2.5 μm deep trenches, the thicker Al_2O_3 coating permitted less light to transmit, as expected since increased coating thickness would decrease trench width and increase UV absorption by confining light near the high-loss Si cladding. The grating that allowed the highest UV flux to transmit was the sample that did not have any coatings applied.

Table 2. Details of Nanograting Samples, Including Depth, Coating, and Ly-α Transmission

sample	depth (μm)	coating	air core width (nm)	mean trans	std dev
1	2.5	20 nm Pt	35	3.8×10^{-4}	7.4×10^{-6}
2	4.5	10 nm Al_2O_3	55	7.5×10^{-4}	3.0×10^{-5}
3	2.5	15 nm Al_2O_3	45	3.1×10^{-3}	3.4×10^{-5}
4	2.5	10 nm Al_2O_3	55	3.9×10^{-3}	1.4×10^{-4}
5	2.5	none	75	4.3×10^{-3}	2.1×10^{-4}

These promising results demonstrate clear improvement in UV rejection of Si nanogratings through application of ALD coatings, and the trend of decreased transmission follows the results of simulated structures. However, the lowest transmission intensity measured, 3.8×10^{-4}, is approximately an order of magnitude higher than the results achieved by the MENA sensor's Au gratings. While some of the variation could be accounted for by the presence of visible light in the experimental setup and air slit width variations caused by the Si etch, the presence of defects in the Si sample created during the fabrication and testing process can also lead to greatly increased transmission. Figure 4 shows a fabricated grating mounted on

dx.doi.org/10.1021/ph500018b | ACS Photonics 2014, 1, 554−559

an aperture plate for testing with visible defects where light is passing unimpeded through the sample. Similar surface defects in Au gratings were plugged by using electroplating, but this process has not yet been attempted for Si nanograting structures. Given the amount of visible defects on fabricated Si structures, a similar defect plugging technique and improvements in fabrication cleanliness and handling could lead to ALD-coated Si nanogratings with orders of magnitude improvement in UV rejection over similar Au grating structures.

CONCLUSION

This work demonstrates improvements in the UV rejection capability of free-standing Si nanograting structures by utilizing ALD coatings. Since Si has metallic optical properties such as EUV wavelengths, metal−insulator−metal plasmon slot waveguide theory was utilized to predict an ideal structure for blocking Ly-α UV while allowing particles to pass through the grating structure. Since high-aspect-ratio nanograting fabrication has run into limitations in patterning ideal trench widths and heights, ALD coating was shown to significantly improve UV extinction by reducing trench width and confining optical fields near the cladding surface. Free-standing Si nanograting structures with a variety of dimensions and ALD coatings were fabricated, and while issues with measurement setup and fabrication defects produced nonideal conditions, expected reduction in UV transmission was achieved that agreed with the theoretical understanding presented. While focusing on a particular application for space-based particle sensors, this work could possibly be used to investigate Si as UV-polarizer material for EUV wavelengths, possibly finding applications in next-generation photolithography. Fabrication methods could also be further used to generate a variety of high-aspect-ratio, ALD-coated nanostructures using a Si backbone.

AUTHOR INFORMATION

Corresponding Authors

*E-mail: thomasz@umich.edu.

*E-mail: guo@umich.edu.

Notes

The authors declare no competing financial interest.

ACKNOWLEDGMENTS

The authors would like to thank Lei Chen at NIST for Pt deposition on the nanograting samples. This research was funded under NASA PIDDP grant NNX09AN25G.

REFERENCES

(1) Pollock, J.; Asamura, K.; Baldonado, J.; Balkey, M. M.; Barker, P.; Burch, J. L.; Korpela, E. J.; Cravens, J.; Dirks, G.; Fok, M.-C.; Funsten, H. O.; Grande, M.; Gruntman, M.; Hanley, J.; Jahn, J.-M; Jenkins, M.; Lampton, M.; Marckwordt, M.; McComas, D. J.; Mukai, T.; Penegor, G.; Pope, S.; Ritzau, S.; Schattenburg, M. L.; Scime, E.; Skoug, R.; Spurgeon, W.; Stecklein, T.; Storms, S.; Urdiales, C.; Valek, P.; van Beek, J. T. M.; Weidner, S. E.; Wüest, M.; Young, M. K.; Zinsmeyer, C. Medium energy neutral atom (MENA) imager for the IMAGE mission. *Space Sci. Rev.* **2000**, *91*, 113−154.

(2) Zurbuchen, T.; Bochsler, P. A.; Scholze, F. Reflection of ultraviolet light at 121.6 nm from rough surfaces. *Opt. Eng.* **1995**, *34*, 1303−1315.

(3) Mukherjee, P.; Kang, M. G.; Zurbuchen, T. H.; Guo, L. J.; Herrero, F. A. Fabrication of high aspect ratio Si nanogratings with smooth sidewalls for a deep UV-blocking particle filter. *J. Vac Sci. Technol. B* **2007**, *25*, 2645−2648.

(4) Moore, T. E.; Chornay, D. J.; Collier, M. R.; Herrero, F. A.; Johnson, J.; Johnson, M. A.; Keller, J. W.; Laudadio, J. F.; Lobell, J. F.; Ogilvie, K. W.; Rozmarynowski, P.; Fuselier, S. A.; Ghielmetti, A. G.; Hertzberg, E.; Hamilton, D. C.; Lundgren, R.; Wilson, P.; Walpole, P.; Stephen, T. M.; Peko, B. L.; van Zyl, B.; Wurz, P.; Quinn, J. M.; Wilson, G. R. The low-energy neutral atom imager for IMAGE. *Space Sci. Rev.* **2000**, *91*, 155−195.

(5) Gruntman, M. Extreme-ultraviolet radiation filtering by free-standing transmission gratings. *Appl. Opt.* **1995**, *34*, 5732−5737.

(6) Gruntman, M. Transmission grating filtering of 52−140 nm radiation. *Appl. Opt.* **1997**, *36*, 2203−2205.

(7) van Beek, J. T. M.; Fleming, R. C.; Hindle, P. S.; Prentiss, J. D.; Schattenburg, M. L.; Ritzau, S. Nanoscale freestanding gratings for ultraviolet blocking filters. *J. Vac. Sci. Technol. B* **1998**, *16*, 3911−3916.

(8) Mukherjee, P.; Zurbuchen, T.; Guo, L. J. Fabrication and testing of freestanding Si nanogratings for UV filtration on space-based particle sensors. *Nanotechnology* **2009**, *20*, 325301.1−325301.8.

(9) Mukherjee, P.; Bruccoleri, A.; Heilmann, R. K.; Schattenburg, M. L.; Kaplan, A. F.; Guo, L. J. Plasma etch fabrication of 60:1 aspect ratio silicon nanogratings with 200 nm pitch. *J. Vac Sci. Technol. B* **2010**, *28*, C6P70−C6P75.

(10) Wan, J.; Kaplan, A. F.; Zheng, J.; Han, X.; Chen, Y.; Weadock, N. J.; Faenza, N.; Li, T.; Guo, L. J.; Hu, L. Two dimensional silicon nanowalls for lithium ion batteries. *J. Mater. Chem. A* **2014**, *2*, 6051−6057.

(11) Palik, E.D. *Handbook of Optical Constants of Solids*, Vol. *1*; Palik, E. D., Ed.; Academic Press: San Diego, USA, 1985.

(12) Palik, E. D. *Handbook of Optical Constants of Solids*, Vol. *2*; Palik, E. D., Ed.; Academic Press: San Diego, USA, 1991.

(13) Hinz, H. J.; Raether, H. Line shape of volume plasmons of silicon and germanium. *Thin Solid Films* **1979**, *58*, 281−284.

(14) Dionne, J. A.; Sweatlock, L. A.; Atwater, H. A.; Polman, A. Plasmon slot waveguides: toward chip-scale propagation with subwavelength-scale localization. *Phys. Rev. B* **2006**, *73*, 35407.1−35407.9.

(15) Zia, R.; Selker, M. D.; Catrysse, P. B.; Brongersma, M. L. Geometries and materials for subwavelength surface plasmon modes. *J. Opt. Soc. Am. A* **2004**, *21*, 2442−2446.

(16) Dionne, J. A.; Lezec, H. J.; Atawater, H. A. Highly confined photon transport in subwavelength metallic slot waveguides. *Nano Lett.* **2006**, *6*, 1928−1932.

(17) Miyazaki, H. T.; Kurokawa, Y. Squeezing visible light waves into a 3-nm-thick and 55-nm-long plasmon cavity. *Phys. Rev. Lett.* **2006**, *96*, 097401.1−097401.4.

(18) Kurokawa, Y.; Miyazaki, H. T. Metal-insulator-metal plasmon nanocavities: analysis of optical properties. *Phys. Rev. B* **2007**, *75*, 035411.1−035411.13.

(19) George, S. M. Atomic layer deposition: an overview. *Chem. Rev.* **2012**, *110*, 111−131.

(20) Kang, G. G.; Vartiainen, I.; Bai, B. F.; Tuovinen, H.; Turunen, J. Inverse polarizing effect of subwavelength metallic gratings in deep ultraviolet band. *Appl. Phys. Lett.* **2011**, *99*, 071103.1−071103.3.

(21) Lehmuskero, A.; Bai, B. F.; Vahimaa, P.; Kuittinen, M. Wire-grid polarizers in the volume plasmon region. *Opt. Express* **2009**, *17*, 5481−5489.

(22) Kong, X. T.; Yan, W. G.; Li, Z. B.; Tian, J. G. Optical properties of metal-multi-insulator-metal plasmonic waveguides. *Opt. Express* **2012**, *20*, 12133−12146.

(23) Guo, L. J. Nanoimprint lithography: method and material requirements. *Adv. Mater.* **2007**, *19*, 495−513.

(24) Okabe, H. Intense resonance line sources for photochemical work in the vacuum ultraviolet region. *J. Opt. Soc. Am.* **1964**, *54*, 478−481.